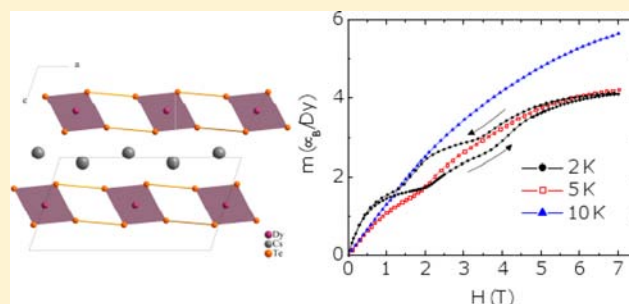


Synthesis, Structure, Magnetism, and Optical Properties of $\text{Cs}_2\text{Cu}_3\text{DyTe}_4$ Jean-Marie Babo,[‡] Eun Sang Choi,[§] and Thomas E. Albrecht-Schmitt^{*,†}[†]Department of Chemistry and Biochemistry, Florida State University, 102 Varsity Way, Tallahassee, Florida 32306-4390, United States[‡]Department of Civil Engineering and Geological Sciences and Department of Chemistry and Biochemistry, University of Notre Dame, Notre Dame, Indiana 46556, United States[§]Department of Physics and National High Magnetic Field Laboratory, Florida State University, Tallahassee, Florida 32310, United States

Supporting Information

ABSTRACT: $\text{CsCu}_3\text{DyTe}_4$ was prepared by reacting copper, dysprosium, and tellurium with cesium azide at 850 °C in a fused silica ampule. This new telluride crystallizes in the monoclinic space group $C2/m$ with lattice dimensions of $a = 16.462(4)$ Å, $b = 4.434(1)$ Å, $c = 8.881(2)$ Å, $\beta = 108.609(12)^\circ$ with $Z = 2$. Its crystal structure is dominated by ${}^2_{\infty}\{[\text{Cu}_3\text{DyTe}_4]\}^{1-}$ anionic layers separated by Cs^+ cations. The copper cations are disordered over three different tetrahedral sites. The $[\text{DyTe}_6]^{9-}$ polyhedra form infinite ${}^1_{\infty}\{[\text{DyTe}_4]^{5-}\}$ chains. Magnetism studies conducted on this semiconductor suggest complex magnetic interactions between the Dy^{3+} cations with a strong deviation from Curie-type behavior at low temperatures below 40 K.



INTRODUCTION

Quaternary A/M/Ln/Q (A = alkali or alkaline-earth metal, M = coinage metal, Ln = rare-earth metal, Q = chalcogen) materials have been extensively studied primarily for their rich structural chemistry. Members of this family include $\text{A}_3\text{Cu}_5\text{Ln}_4\text{Te}_{10}$ (A = K–Cs; Ln = Sm, Gd, Er),^{1,2} $\text{CsCuGd}_2\text{Te}_4$,³ $\text{CsCu}_2\text{Sc}_3\text{Te}_6$,⁴ BaMLnTe_3 (M = Cu, Ag; Ln = La, Gd, Yb),^{1,5} $\text{K}_2\text{Ag}_3\text{CeTe}_4$,⁶ $\text{Cs}_{0.73}\text{Cu}_{5.27}\text{Pr}_2\text{Te}_6$,⁷ $\text{RbCu}_3\text{CeTe}_5$,⁸ KCuCeTe_4 ,⁹ $\text{KCu}_2\text{EuTe}_4$, and $\text{Na}_{0.2}\text{Ag}_{2.8}\text{EuTe}_4$.¹⁰ These compounds exhibit a wide variety of lanthanide chalcogenide topologies from chains in $\text{K}_2\text{Ag}_3\text{CeTe}_4$ to layers in $\text{CsCu}_2\text{Sc}_3\text{Te}_6$ to three-dimensional networks in $\text{CsCuGd}_2\text{Te}_4$. Channel structures where the alkali metal or alkaline-earth metals reside in the channels are particularly prevalent.^{1–6} The Eu^{3+} members of this family have particularly rich structural chemistry, and $\text{KCu}_2\text{EuTe}_4$ and $\text{Na}_{0.2}\text{Ag}_{2.8}\text{EuTe}_4$ both possess superlattices with charge-density waves. Physical property measurements on this family are not well-developed. However, $\text{K}_2\text{Ag}_3\text{CeTe}_4$ is a narrow band gap semiconductor with a large Seebeck coefficient, making it a promising thermoelectric material. Dysprosium phases are limited to BaDyCuTe_3 , $\text{K}_{1.5}\text{Dy}_2\text{Cu}_{2.5}\text{Te}_5$, and $\text{K}_{0.5}\text{Ba}_{0.5}\text{DyCu}_{1.5}\text{Te}_3$.¹ These compounds have only been structurally characterized, but $\text{K}_{0.5}\text{Ba}_{0.5}\text{DyCu}_{1.5}\text{Te}_3$ adopts a polar structure (space group $Cmc2_1$), which gives rise to the possibility of using it as a nonlinear optical material with applications in the NIR.¹¹

In this work we report the structure, magnetism, and heat capacity measurements of the new lanthanide-poor quaternary telluride, $\text{Cs}_2\text{Cu}_3\text{DyTe}_4$, which has the same stoichiometry and

is structurally related to $\text{K}_2\text{Ag}_3\text{CeTe}_4$.⁶ These compounds have rather simple structure descriptions in that they contain chains of edge-sharing LnTe_6 octahedra that are joined together by coinage metal polyhedra to form anionic layers that are separated from one another by alkali metal cations. These compounds are promising for attaining magnetic ordering because they possess a short crystallographic axis that the LnTe_6 chains extend along giving rise to a short Ln...Ln contact. Herein we demonstrate that this leads to complex magnetic interactions in $\text{Cs}_2\text{Cu}_3\text{DyTe}_4$.

EXPERIMENTAL SECTION

Synthesis. $\text{Cs}_2\text{Cu}_3\text{DyTe}_4$ was prepared by the reaction of Dy, Cu, Te, and CsN_3 (as cesium source). The mixture of 0.350 mg (0.2 mmol) of CsN_3 , 0.191 mg (0.3 mmol) of Cu, 0.163 mg (0.1 mmol) of Dy, and 0.511 mg (0.4 mmol) of Te was loaded into a fused silica ampule under an argon atmosphere. The tube was then evacuated, torch-sealed, and placed in a furnace. The latter was slowly heated to 400 °C over 24 h followed by fast heating to 850 °C over 3 h where it was maintained for 5 days, and then finally cooled down to room temperature at the rate of 10 °C/h. The chemicals were used as received, and since cesium azide melts at 310 °C and starts decomposition before 400 °C, the chemical reaction expected is: $2\text{CsN}_3 + 3\text{Cu} + 4\text{Te} \rightarrow \text{Cs}_2\text{Cu}_3\text{DyTe}_4 + 3\text{N}_2$. This compound was first synthesized by reacting stoichiometric amount of Cu, Dy, Te in excess of CsCl as flux at 850 °C, but the yield was very low. As with

Received: July 27, 2012

Published: October 5, 2012

most tellurides, this compound is stable in moist air for only a few weeks.

Elemental Analysis. The semiquantitative elemental analyses of $\text{Cs}_2\text{Cu}_3\text{DyTe}_4$ was examined on the field emission scanning electron microprobe (LEO EVO 50) equipped with an Oxford INCA energy dispersive X-ray spectrometer (EDX).

Structure Determination. A black block-shaped single crystal corresponding to $\text{Cs}_2\text{Cu}_3\text{DyTe}_4$ was isolated for single crystal X-ray analysis, and data were collected with the use of graphite monochromated Mo $K\alpha$ radiation ($\lambda = 0.71073 \text{ \AA}$) at room temperature on Bruker APEXII CCD X-ray diffractometer. SAINT software¹² was used for data integration including Lorentz and polarization corrections. The absorption corrections were done using the SADABS program. The structure solution and refinement for the title compound was performed with the aid of the SHELXTL package of crystallographic programs.¹³ The complete data collection parameters and details of the structure solutions and refinements are summarized in Table 1, while in Tables 2 and 3 the positional coordinates and isotropic equivalent thermal parameters are given, respectively.

Table 1. Crystallographic Data of $\text{Cs}_2\text{Cu}_3\text{DyTe}_4$

compd	$\text{Cs}_2\text{Cu}_3\text{DyTe}_4$
cryst syst	monoclinic
space group	$C2/m$ (No. 14)
unit cell parameters, $a/\text{\AA}$	16.462(4)
$b/\text{\AA}$	4.434(1)
$c/\text{\AA}$	8.881(2)
β/deg	108.609(12)
formula unit per unit cell (Z)	2
calcd density (D_x in g/cm^3)	5.76
molar volume (V_m in cm^3/mol)	184.98
index range ($\pm h_{\text{max}}/\pm k_{\text{max}}/\pm l_{\text{max}}$)	21/5/11
$2\theta_{\text{max}}$ (deg)	55.01
$F(000)$	942
abs coeff (μ in mm^{-1})	26.22
collected reflns	5160
unique reflns	788
$R_{\text{int}}/R_{\sigma}$	0.036/0.024
reflns with $ F_o \geq 4\sigma(F_o)$	788
$R1/R1$ with $ F_o \geq 4\sigma(F_o)$	0.024/0.022
wR2 (for all reflns)	0.045
GOF	1.156
residual electron density (max/min) (ρ in $\text{e}^- \times 10^6 \text{ pm}^{-3}$)	1.55/−1.21

Powder X-ray Diffraction. Powder X-ray diffraction patterns were collected with a Scintag theta–theta diffractometer equipped with a diffracted-beamed monochromatic set for $\text{CuK}\alpha$ ($\lambda = 1.5418 \text{ \AA}$).

Magnetism and Heat Capacity. Direct current susceptibility and magnetization data were measured on powder samples in polycarbonate sample holders with a Quantum Design MPMS between 2 and 300 K and in applied fields up to 7 T. Direct current susceptibility measurements were measured under zero-field-cooled (ZFC) or field-cooled (FC) conditions. The heat capacity measurement was done on

Table 3. Selected Bond Distances (in \AA) in $\text{Cs}_2\text{Cu}_3\text{DyTe}_4$

Dy–Te1($\times 4$)	3.074(1)	Cu1–Te1($\times 1$)	2.666(1)
–Te2($\times 2$)	3.164(1)	–Te2($\times 2$)	2.711(1)
		–Te2'($\times 1$)	2.809(1)
Cs–Te1($\times 2$)	3.784(2)	Cu2–Te1($\times 1$)	2.561(1)
–Te2($\times 2$)	3.757(1)	–Te2($\times 2$)	2.601(1)
–Te1'($\times 2$)	3.919(2)	Cu3–Te2($\times 1$)	2.484(1)
–Te2'($\times 1$)	3.865(2)	–Te2'($\times 1$)	2.656(1)
		–Te1($\times 1$)	2.672(1)
Dy–Cu	2.930(2)	Cu1–Cu2	2.026(2)
Cs–Cu	3.835(2)	Cu1–Cu3	0.553(2)
Dy–Dy	4.434(2)	Cu3–Cu3	0.768(2)
		Cu2–Cu3	2.444(2)

a pelleted sample using a Quantum Design PPMS. N grease was used as thermal glue to the sample stage, whose contribution to the total heat capacity was measured before the sample was mounted.

UV–Vis–NIR Diffuse Reflectance Spectroscopy. The reflectance spectrum of the title compound was collected from a single crystal at room temperature using a Craic Technologies UV–vis–NIR microspectrometer. The reflectance data that were collected were used to estimate the material's band gap as reflectance is converted into absorption via the Kubelka–Munk function: $\alpha/S = (1 - R)^2/2R$, where α is absorption coefficient, S the scattering coefficient, and R the reflectance.

RESULTS

Crystal Structure. The $\text{Cs}_2\text{Cu}_3\text{DyTe}_4$ crystal structure is composed of ${}_{\infty}^2\{[\text{Cu}_3\text{DyTe}_4]\}^{1-}$ anionic layers with Cs^+ cations residing between the layers. A view of the crystal structure of $\text{Cs}_2\text{Cu}_3\text{DyTe}_4$ is shown in Figure 1. The basic units that make

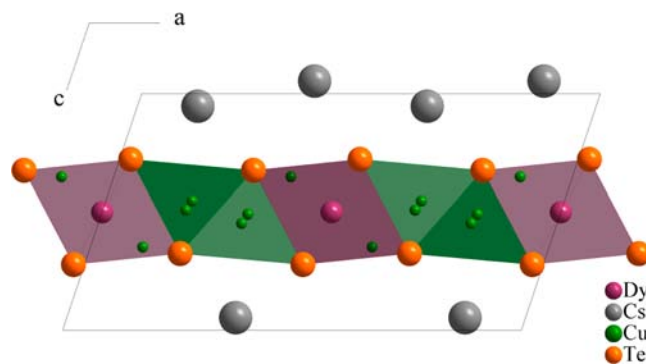


Figure 1. $\text{Cs}_2\text{Cu}_3\text{DyTe}_4$ crystal structure viewed along the b -axis.

up the anionic layers are $[\text{DyTe}_6]^{9-}$ and $[\text{CuTe}_4]^{7-}$ polyhedra. The dysprosium telluride octahedra share trans-edges to form isolated infinite chains extending along the short b -axis. These chains are packed into layers parallel to $[010]$ and generate large twisted octahedral gaps between them (Figure 2). These

Table 2. Atomic Coordinates and Equivalent Thermal Parameters for $\text{Cs}_2\text{Cu}_3\text{DyTe}_4$

atoms	SOF	Wyckoff site	x/a	y/b	z/c	U_{eq}
Cs	1	4i	0.36810(3)	0	−0.05320(6)	0.0209(2)
Dy	1	2d	$1/2$	0	$1/2$	0.0269(2)
Cu1	0.5	4i	0.6807(4)	$-1/2$	0.4914(8)	0.0287(10)
Cu2	0.5	4i	0.61399(15)	$-1/2$	0.6478(3)	0.0325(6)
Cu3	0.25	8j	0.6878(5)	−0.4130(30)	0.4526(6)	0.0546(23)
Te1	1	4i	0.52420(3)	$-1/2$	0.27828(10)	0.0147(2)
Te2	1	4i	0.29980(3)	0	0.32473(7)	0.0169(2)

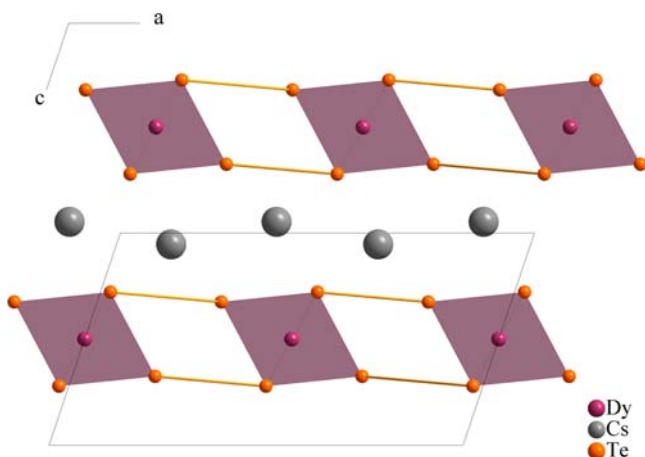


Figure 2. ${}^1_{\infty}\{[\text{DyTe}_4]^{5-}\}$ single chains sitting into layers stacked perpendicularly to $[001]$ and generating distorted octahedral structures within layers.

strongly distorted octahedral voids also host four tetrahedral sites but only accommodate two copper sites (Figure 3, left).

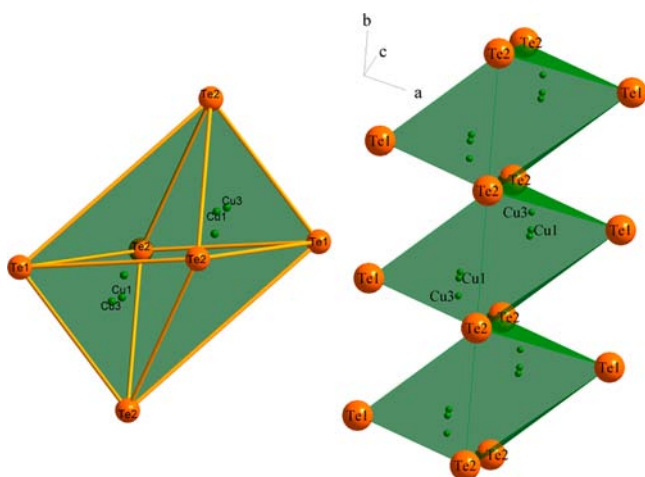


Figure 3. $[\text{Te}_6]$ distorted octahedron containing four tetrahedral sites where only two are disorderly occupied by Cu^+ cations at Cu1 or Cu3 sites (left) and three $[\text{Te}_6]$ -polyhedra sharing trans-edges to form chain (right).

Between the dysprosium telluride chains and the generated octahedral voids there are extra tetrahedral sites that can also contain additional Cu^+ . The copper cations are disordered over these three different tetrahedral sites (Cu1 and Cu3 sites in distorted octahedral voids while Cu2 is in the extra position). The $[\text{CuTe}_4]^{7-}$ polyhedra share edges and corners to form ${}^2_{\infty}\{[\text{Cu}_3\text{Te}_4]^{5-}\}$ layers that stack perpendicular to $[001]$. The Cu–Te layers embed ${}^1_{\infty}\{[\text{DyTe}_4]^{5-}\}$ single chains to form ${}^2_{\infty}\{[\text{Cu}_3\text{DyTe}_4]^{1-}\}$ anionic layers (see Figure 1). The Cs^+ cations are surrounded by seven telluride anions in a monocapped trigonal prism.

Short Cu–Cu distances of 0.55, 0.77, 2.03, and 2.44 Å are direct consequences of the copper atoms disordering over the three different sites. Typical $\text{Cu(I)}\cdots\text{Cu(I)}$ distances are around 2.76 Å and are characteristic of $d^{10}\text{--}d^{10}$ interactions. The Cu–Te bond lengths range from 2.48 and 3.24 Å and are broader compared to those of 2.55–2.77 Å in $\text{CsCuGd}_2\text{Te}_4$,³ 2.66–2.74 Å in BaCuLaTe_3 ,⁵ or those of 2.57–2.80 Å in $\text{BaCu}_{6-y}\text{STe}_4$.¹⁴

The copper centers are found in distorted $[(\text{Cu}_2)\text{Te}_4]^{7-}$ and $[(\text{Cu}_3)\text{Te}_4]^{7-}$ tetrahedra with Te–Cu–Te scattered angles ranging from 95.3° to 123.1°, while the Cu1 polyhedra are much more ideal with Te–Cu–Te angles between 107.7° and 110.5°. The Cu3 site is displaced 0.41 Å above one of the triangular faces, while Cu2 is 0.37 Å with the secondary contacts of 3.24 and 3.14 Å, respectively. The Dy–Te bond lengths are between 3.07 and 3.17 Å (see Table 2) in good agreement with those of 2.99–3.19 Å found in $\text{K}_{1.5}\text{Cu}_2.5\text{Dy}_2\text{Te}_5$,¹ or 3.03–3.13 in BaDy_2Te_4 ,¹⁵ CsZnDyTe_3 ,¹⁶ and CsCdDyTe_3 .¹⁷ The Cu–Te and Dy–Te polyhedra face-share yielding a short distance between Dy and Cu atoms of 2.93 Å. This situation happens when two polyhedra share a common face as observed in $\text{CsCu}_3\text{Sc}_3\text{Te}_6$ [$d(\text{Sc}\cdots\text{Cu}) = 2.83$ Å] or in $\text{CsCuGd}_2\text{Te}_4$ [$d(\text{Gd}\cdots\text{Cu}) = 2.84$ Å]. The nearest Dy \cdots Dy contact is equivalent to the short b -axis at 4.434(2) Å. This is the important distance for magnetic coupling. There are no other short Dy \cdots Dy contacts. The cesium cations residing between the layers are 7-fold coordinated in a monocapped trigonal prism with Cs–Te bond lengths between 3.75 and 3.92 Å, which are somewhat shorter than those of 3.90–4.21 Å in $\text{CsCu}_3\text{Sc}_3\text{Te}_6$ or 3.81–4.34 Å in $\text{CsCuGd}_2\text{Te}_4$. However, the coordination number might justify these bond lengths as seen in layered CsNdTe_2 (Cs–Te = 3.78 Å; CN(Cs) = 6),¹⁸ CsZnNdTe_3 (Cs–Te ranged from 3.79 to 4.19 Å; CN(Cs) = 8),¹⁶ and CsBi_4Te_6 (Cs–Te from 3.76 to 4.19 Å; CN(Cs) = 10)¹⁹ or in the three-dimensional $\text{Cs}_{0.73}\text{Cu}_{5.27}\text{Pr}_2\text{Te}_6$ (Cs2–Te = 3.69 Å; CN(Cs) = 6).¹⁷ The Cs \cdots Cu contact at 3.84 Å is relatively short but not unusual, as similar ones at 3.79 Å have been reported in $\text{CsCu}_3\text{Dy}_2\text{Se}_5$,²⁰ for example.

The crystal structure of $\text{Cs}_2\text{Cu}_3\text{DyTe}_4$ is very close to that of $\text{K}_2\text{Cu}_2\text{CeS}_4$ though its stoichiometry is more similar to that of $\text{K}_2\text{Ag}_3\text{CeTe}_4$.²¹ The latter forms a three-dimensional anionic framework, whereas the title compound forms layers intercalated by Cs^+ cations. Moreover, the silver cations in $\text{K}_2\text{Ag}_3\text{CeTe}_4$ occupy three different tetrahedral positions, while the copper ions are statistically disordered over three different sites. The shortest Te \cdots Te contact is above 4.24 Å, so there is no evidence for Te–Te bonds, and formula can be charge balanced as $(\text{Cs}^+)_2(\text{Cu}^+)_3(\text{Dy}^{3+})(\text{Te}^{2-})_4$.

Optical Properties. UV–vis–NIR reflectance spectroscopy was performed on a single crystal and reveals a band gap of 1.38 eV. This value is also consistent with the observed black color of the crystals. The magnetism contribution in this compound according to the oxidation state of the elements is almost exclusively from the dysprosium cations, even though connections between band gap energy and the Curie temperature in lanthanide chalcogenides have been reported.²² The absorption edge observed at 1.10 eV is typical of lanthanide chalcogenides and is also reported in ref 23.

Magnetism and Heat Capacity. The inverse molar Ln magnetic susceptibilities for $\text{Cs}_2\text{Cu}_3\text{DyTe}_4$ in the range 2–300 K are shown in Figure 4. After subtracting the temperature independent background term (χ_0) from the sample holder and the core diamagnetism, the inverse susceptibility can be fitted to a linear T -dependence for a wide temperature range (30–300 K). From the slope of the linear fitting, the effective magnetic moment was obtained to be 10.3 μ_B , close to that of free Dy^{3+} ion (10.63 μ_B). The fitted Weiss temperature is 9.9 K suggesting antiferromagnetic interaction between the Dy^{3+} ions. At low temperatures, the linear behavior starts to deviate, probably from the crystalline electric field (CEF) effect of Dy^{3+} under octahedral crystalline electric field. An anomaly in the

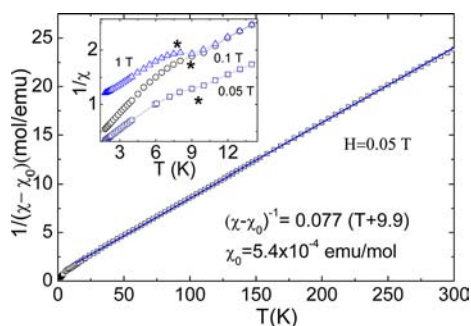


Figure 4. Temperature dependence of inverse susceptibility ($(\chi - \chi_0)^{-1}$) measured at $H = 0.05$ T. The line indicates a linear fitting result for between 30 and 300 K. Inset: $1/\chi(T)$ at low temperatures for $H = 0.05, 0.1,$ and 1 T. The asterisks denote the long-range AFM ordering temperature T_N .

susceptibility is observed around 10 K, which decreases with magnetic field as shown in the inset of Figure 4.

Figure 5 shows the temperature dependence of magnetic moment below 40 K. For the magnetic fields larger than or equal to 2.5 T, the temperature dependence strongly deviates from the Curie-type behavior at low temperatures: (1) temperature independent behavior for the FC, and (2) a broad peak for the ZFC data. As a result, there is a difference between ZFC and FC data, in which the bifurcation temperature is around the peak temperature (T_{peak}).

To further investigate the field induced behavior at low temperatures, we measured magnetization and heat capacity at different conditions of temperatures and fields. Figure 6 shows the magnetization at different temperatures, where magnetization steps are observed for 2 and 5 K data. The magnetization steps appear at 2.0 and 3.7 T for the up sweep and show clear hysteresis between up and down sweeps.

Figure 7 shows the heat capacity data at low temperatures at different magnetic fields of 0, 1, 2.5, and 3 T. There are two notable features in the heat capacity data: (1) heat capacity jump for 0 and 1 T, and (2) no observable heat capacity anomaly for 2.5–4 T data. The temperatures at which the specific heat feature 1 occurs are close to those of the susceptibility anomaly (denoted as asterisks in the inset of Figures 4 and 5). The heat capacity jump is suppressed rapidly with magnetic fields, which is more clearly shown after the lattice contribution of the specific heat is subtracted as shown in

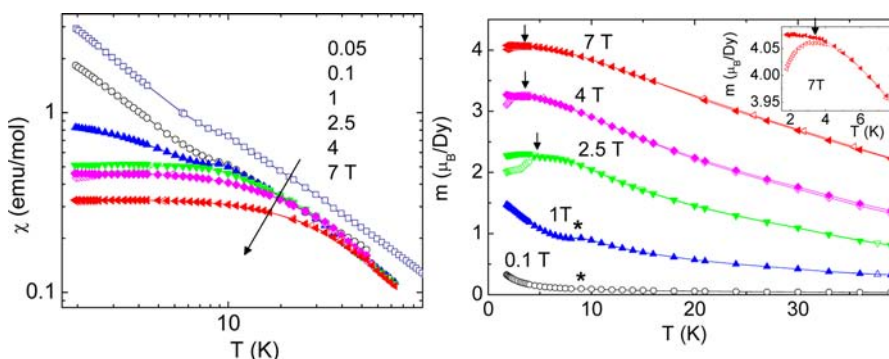


Figure 5. Temperature dependence of magnetic susceptibility in log–log scale (left) and the same data plotted as magnetic moment per Dy^{3+} ion (right) in linear scale at different external fields. Open symbols denote for the ZFC condition and solid symbols for the FC condition. Only ZFC data are shown for 0.05 and 0.1 T data. Inset shows low temperature expansion of 7 T data. The down arrows indicate the temperatures where the magnetic moment shows maxima for the ZFC condition while the asterisks denote T_N (see text).

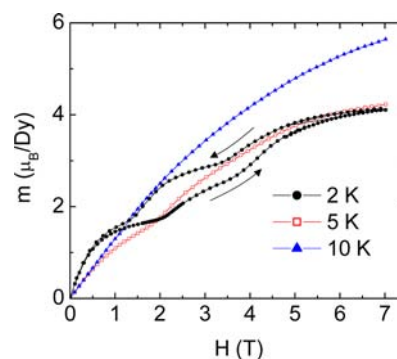


Figure 6. Magnetization data of $\text{Cs}_2\text{Cu}_3\text{DyTe}_4$ at different temperatures. Both up and down sweep data are shown for $T = 2.0$ K.

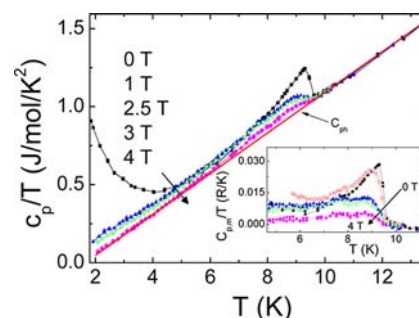


Figure 7. Heat capacity (C_p/T) data at different fields. The solid line indicates the fitted lattice contribution (C_{ph}/T). Inset shows C_p/T data after the lattice contribution was subtracted ($C_{\text{p,m}}/T = C_p/T - C_{\text{ph}}/T$).

the inset of Figure 7. The proximity of the temperatures and its field dependence indicates that the anomaly comes from a long-range antiferromagnetic (AFM) ordering of Dy^{3+} with the Néel temperature (T_N) around 9.5 K. We note that the T_N is also very close to the Weiss temperature (9.9 K) obtained from the modified Curie–Weiss fitting. The entropy change (ΔS) associated with the AFM ordering can be determined from the relation $\Delta S = \int (C_p - C_{\text{ph}})/T \, dT$, where C_{ph} is the lattice contribution to the heat capacity. Using an empirical curve for the lattice contribution shown in Figure 7, we obtained $\Delta S = 0.05R$ ($R = 8.31$ J/K mol). In the case of long-range ordering of magnetic ions with total angular momentum J , ΔS is expressed as $\Delta S = R \ln(2J+1)$. In $\text{Cs}_2\text{Cu}_3\text{DyTe}_4$, $\Delta S = 2.77R$ for a full AFM ordering of Dy^{3+} ($J = 7.5$), which is much larger than the

experimental value. This suggests that only the very small portion of the available Dy^{3+} ions participate in the AFM ordering, which is likely to cause the rather insignificant susceptibility anomaly at T_N .

Combining the results of the magnetic susceptibility and specific heat measurements, a TH -phase diagram is suggested as shown in Figure 8. The dashed line for the field-induced phase

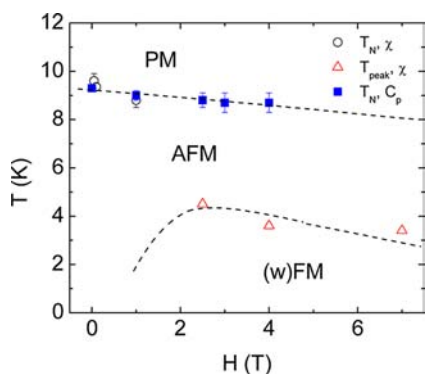


Figure 8. TH phase diagram of $\text{Cs}_2\text{Cu}_3\text{DyTe}_4$. PM, AFM, and (w)FM represent for paramagnetic, antiferromagnetic, and (weak) ferromagnetic state, respectively. The dashed lines are guides to the eyes (see text).

was drawn from the peak temperatures of the ZFC susceptibility and from an assumption that the field-induced phase exists at temperatures below 2 K for $H = 1$ T. This assumption is reasonable considering the magnetization hysteresis measured at 2 K persists down to 1 T (see Figure 6). One can speculate that the absence of clear evidence of a long-range ordering from the heat capacity measurement can be the consequence of the fact that the field-induced phase is located inside the AFM phase.

The identification of the field-induced phase is not currently well understood. The steplike increase of the magnetization and the hysteresis resembles itinerant metamagnetism, where itinerant ferromagnetism is field-induced from the low field AFM or PM state. This scenario could also explain the temperature dependence of susceptibility at low temperatures and the difference between ZFC and FC data. However, the susceptibility in the field-induced phase is too small for a ferromagnetic state and the optical measurement results clearly indicate that $\text{Cs}_2\text{Cu}_3\text{DyTe}_4$ is band-gapped semiconductor, inconsistent with the itinerant magnetism scenario. Another possible scenario is weak ferromagnetism due to anisotropic exchange coupling (Dzyaloshinskii-Moriya (DM) interaction) due to spin-orbit coupling.^{24,25} In this scenario, the antiferromagnetically ordered moments are canted to a certain direction under external magnetic fields resulting in ferromagnetic moments. The canting occurs when the field exceeds certain threshold value to overcome the antiferromagnetic interaction, hence the step-like magnetization jump and the hysteresis behavior. The two magnetization steps shown in Figure 6 suggest that canting involves two processes with different threshold magnetic fields. More experiments, such as neutron diffraction, AC susceptibility, expanding the phase diagram to higher fields and lower temperatures are needed to examine the scenarios mentioned above. Especially for the weak ferromagnetism, magnetic property measurements on single crystal samples, if available, will provide useful information to

identify the easy axes of the antiferromagnetism, weak ferromagnetism and the DM vector.

CONCLUSIONS

$\text{Cs}_2\text{Cu}_3\text{DyTe}_4$ can be prepared via the reaction of the elements with cesium azide. The compound forms a layered structure with Cs^+ cations separating the layers. The anionic layers are assembled from chains of $[\text{DyTe}_6]^{9-}$ octahedra and disordered Cu^+ cations. The most important feature of the structure is the short Dy...Dy contact that gives rise to antiferromagnetic ordering at low temperatures. The differences between the ZFC and FC magnetic susceptibility data indicate that exact nature of the ordering is complex and inconsistent with simple models. Hopefully future neutron diffraction measurements will shed some light on this complexity.

ASSOCIATED CONTENT

Supporting Information

CIF data. This material is available free of charge via the Internet at <http://pubs.acs.org>.

AUTHOR INFORMATION

Corresponding Author

*E-mail: talbrechtschmitt@gmail.com.

Notes

The authors declare no competing financial interest.

REFERENCES

- Huang, F.-Q.; Choe, W.-Y.; Chu, J. S. *Chem. Mater.* **1998**, *10*, 1320.
- Huang, F.-Q.; Ibers, J. A. *J. Solid State Chem.* **2001**, *160*, 409.
- Babo, J.-M.; Strobel, S.; Schleid, T. *Z. Anorg. Allg. Chem.* **2010**, *636*, 349.
- (a) Babo, J.-M.; Schleid, T. *J. Solid State Sci.* **2010**, *12*, 238–245.
(b) Babo, J.-M.; Hartenbach, L.; Schleid, T. *Z. Kristallogr.* **2007**, *Suppl.* *25*, 19.
- Yang, Y.-T.; Ibers, J. A. *J. Solid State Chem.* **1999**, *147*, 409.
- Patschke, R.; Brazis, P.; Kannewurf, C. R.; Kanatzidis, M. G. *Inorg. Chem.* **1998**, *37*, 6562.
- Meng, C.-Y.; Chen, H.; Wang, P.; Chen, L. *Chem. Mater.* **2011**, *23*, 4910.
- Patschke, R.; Brazis, P.; Kannewurf, C. R.; Kanatzidis, M. G. *J. Mater. Chem.* **1998**, *8*, 2587.
- Patschke, R.; Heising, J.; Kanatzidis, M. G. *Chem. Mater.* **1998**, *10*, 695.
- Patschke, R.; Brazis, P. C.; Kannewurf, R.; Kanatzidis, M. G. *J. Mater. Chem.* **1999**, *9*, 2293.
- Zhao, Y.-X.; Burda, C. *Energy Environ. Sci.* **2012**, *5*, 5564.
- SAINT: Version 4; Siemens Analytical X-ray Systems, Inc.: Madison, WI, 1994–1996.
- Sheldrick, G. M. *SHELXTL: Version 5*; Siemens Analytical X-ray Systems, Inc.: Madison, WI, 1994.
- Mayasree, O.; Sankar, C. R.; Assoud, A.; Kleinke, H. *Inorg. Chem.* **2011**, *50*, 4580.
- Narducci, A. A.; Yang, Y.-T.; Digman, M. A.; Sipes, A. B.; Ibers, J. A. *J. Alloys Compd.* **2000**, *303*, 432.
- Liu, Y.; Chen, L.; Wu, L.-M.; Chan, G.-H.; van Duynne, R. P.; Ibers, J. A. *Inorg. Chem.* **2008**, *47*, 855.
- Yao, J.; Deng, B.; Sherry, J. L.; McFarland, A. D.; Ellis, D. E.; van Duynne, R. P. *Inorg. Chem.* **2004**, *43*, 7735.
- Stoewe, K.; Napoli, C.; Appel, S. *Z. Anorg. Allg. Chem.* **2003**, *629*, 1925.
- Chung, D.-Y.; Hogan, T. P.; Rocci-Lane, M.; Brazis, P.; Ireland, J. R.; Kannewurf, C. R.; Bastea, M.; Uher, C.; Kanatzidis, M. G. *J. Am. Chem. Soc.* **2004**, *126*, 6414.
- Strobel, S.; Schleid, T. *Z. Anorg. Allg. Chem.* **2004**, *630*, 706.

- (21) Sutorik, A. C.; Albritton-Thomas, J.; Kannewurf, C. R.; Kanatzidis, M. G. *J. Am. Chem. Soc.* **1994**, *116*, 751.
- (22) Regulacio, M. D.; Bussmann, K.; Lewis, B.; Stoll, S. L. *J. Am. Chem. Soc.* **2006**, *128*, 11173.
- (23) Babo, J.-M.; Albrecht-Schmitt, T. E. *J. Solid State Chem.* **2012**, *187*, 264.
- (24) Dzyaloshinskii, I. *J. Phys. Chem. Solids* **1958**, *4*, 241.
- (25) Moriya, T. *Phys. Rev.* **1960**, *120*, 91.